

Article

# Defect Creation in the Root of Single-Crystalline Turbine Blades Made of Ni-Based Superalloy

Jacek Krawczyk <sup>1</sup>, Robert Paszkowski <sup>1,\*</sup>, Włodzimierz Bogdanowicz <sup>1</sup>,  
Aneta Hanc-Kuczkowska <sup>1</sup>, Jan Sieniawski <sup>2</sup> and Bartosz Terlecki <sup>1</sup>

<sup>1</sup> Institute of Materials Science, University of Silesia in Katowice, 1A 75 Pulku Piechoty St., 41-500 Chorzów, Poland; jacek.krawczyk@us.edu.pl (J.K.); wlodzimierz.bogdanowicz@us.edu.pl (W.B.); aneta.hanc@us.edu.pl (A.H.-K.); bterlecki@us.edu.pl (B.T.)

<sup>2</sup> Department of Materials Science, Rzeszow University of Technology, 2 Wincentego Pola St., 35-959 Rzeszów, Poland; jansien@prz.edu.pl

\* Correspondence: robert.paszkowski@us.edu.pl; Tel.: +48-32-349-75-36

Received: 31 January 2019; Accepted: 12 March 2019; Published: 15 March 2019



**Abstract:** An analysis of the defects in the vicinity of the selector–root connection plane occurring during the creation of single-crystalline turbine blades made of CMSX-6 Ni-based superalloy was performed. X-ray diffraction topography, scanning electron microscopy, and positron annihilation lifetime spectroscopy were used. Comparing the area of undisturbed axial growth of dendrites to the area of lateral growth concluded that the low-angle boundaries-like (LAB-like) defects were created in the root as a result of unsteady-state lateral growth of some secondary dendrite arms in layers of the root located directly at the selector–root connection plane. Additional macroscopic low-angle boundaries (LABs) with higher misorientation angles were created as a result of concave curvatures of liquidus isotherm in platform-like regions near selector–root connections. Two kinds of vacancy-type defects, mono-vacancies and vacancy clusters, were determined in relation to the LABs and LAB-like defects. Only mono-vacancies appeared in the areas of undisturbed axial growth. Reasons for the creation of macroscopic LABs and LAB-like defects, and their relationships with vacancy-type defects were discussed.

**Keywords:** superalloy; Bridgman technique; positron annihilation lifetime spectroscopy (PALS); vacancy-type defects; X-ray topography; defects; lateral growth; dendrite array; low-angle boundaries

## 1. Introduction

It is known that many types of defects in single-crystalline (SX) turbine blades are created during directional crystallization by the Bridgman technique, while the crystallization front passes through areas with abrupt changes in a geometry of the cast [1–8]. The layers of the blade root located near the plane of connection with a selector (selector-root (S–R) connection), where branching of the primary dendrite arms and lateral growth occur, are especially important for defects creation [9–14]. In these layers, the low-angle boundaries (LABs), related to the local crystal misorientation, are created [15]. The LABs formed in the layers of the root, located near the plane of the S–R connection, may be inherited by the entire root and also by the airfoil [16,17]. The LABs are difficult or impossible to eliminate by heat treatment in subsequent stages of the blade’s production [18]. Furthermore, in some layers of the root located near the plane of the S–R connection, the dendrites grow in an unsteady regime, and additional defects such as dislocations and non-equilibrium vacancies may be created. Therefore, it is necessary to test for defects in the root layers located in the vicinity of the plane of the S–R connection and to analyze how they were created. The density of dislocations and vacancy-type defects are important for creep processes in Ni-based single-crystalline superalloys [19].

Studies of defects created by lateral growth may be performed by comparing defect structure areas created by undisturbed axial growth and the areas beyond it. Undisturbed dendrite growth occurs in the root area of the selector extension (SE, Figure 1a,b) as opposed to the neighboring areas (L, Figure 1b). The study of defects created during lateral dendrite growth are important, especially for the recently developed methods for obtaining single-crystalline casts, e.g., the liquid metal cast (LMC) method for SX cast production [20]. Disturbances in the expected crystallographic orientation may cause reduction in strain properties [21].

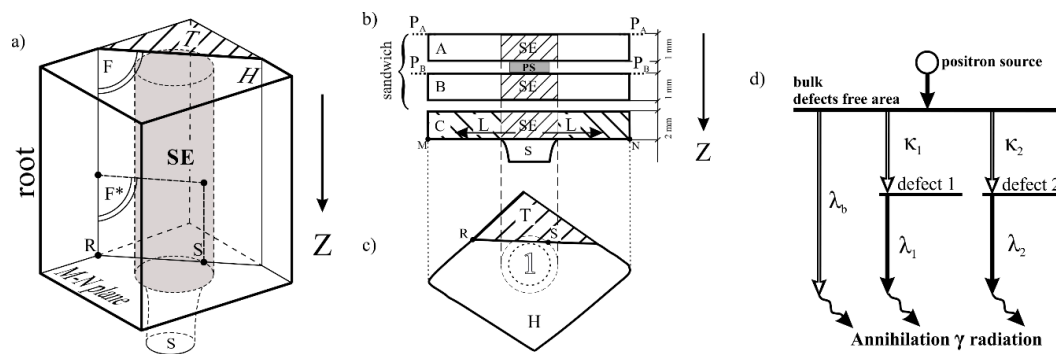


**Figure 1.** (a) Cut-off scheme of the root fragment T by plane F parallel to the withdrawal axis Z and the sections shape of the specimens of fragment H (b) parallel and (c) perpendicular to Z.  $P_A$ – $P_A$  and  $P_B$ – $P_B$ —the surfaces from which the X-ray topograms were obtained, PS—the positron source for positron annihilation lifetime spectroscopy (PALS) measurements in area 1, S—selector, SE—selector extension area of the root; (d) scheme of the positron annihilation processes according to the three-state trapping model. Horizontal lines represent the delocalized state of positron in bulk material (defect-free area) and its two localized states on two types of defects.  $\lambda_b$  is the annihilation rate of the delocalized (free) positron in the bulk,  $\lambda_1$  and  $\lambda_2$ —the annihilation rates in two different types of defects.  $\kappa_1$  and  $\kappa_2$ —the trapping rates in defects.

The defects in SX casts related to the local change of crystal orientation in macroscopic areas, e.g., macroscopic LABs or local change in the crystal interplanar spacing in these areas, may be visualized by X-ray reflective topography [22]. This method allows to indicate the macroscopic areas in which the changes in type and density of such defects as dislocations or vacancies may occur. All these changes may be specified by positron annihilation lifetime spectroscopy (PALS), which allows to obtain parameters of the macroscopic areas and is especially sensitive to vacancy-type defects. The common application of these two methods may allow to find a relation between the LABs and vacancy-type defects.

The PALS method, described in detail by Reference [23], is an exceptionally good method for the simultaneous determination of concentration and type of defects. The current PALS studies of Ni-based compounds are related to the characteristics of defects in  $Ni_3Al$ -based alloys and in poly-crystalline Ni-based superalloys [24–28]. However, there are no PALS studies regarding investigations of defects in fragments of single-crystalline turbine blades.

The concentration of vacancy-type defects in multicomponent technical superalloys containing many alloying elements is particularly important because it is related to the kinetics of diffusion processes [29,30]. For example, it can determine the kinetics of the  $\gamma \rightarrow \gamma'$  solid-solution transformation during the Bridgman process or during heat treatment of SX turbine blades. The dendritic segregation of alloying elements is one of the reasons for the heterogeneity concentration of vacancy-type defects. The heterogeneity of vacancy-type defects concentration, especially the vacancy clusters, may be related to the pore distribution in as-cast blades [31]. Exceeding the critical concentration of the vacancies in the  $\gamma$  phase may cause creation of undesirable TCP phases [30,32]. On the other hand, the LABs, easily visualized by X-ray diffraction topography, are equally important because dislocations in LABs may play a role as sources or sinks for the vacancies. Additionally, in superalloys with the

addition of W and Re (2nd and 3rd generations such as CMSX-4 and CMSX-10), the elements can also cause a specific phase instability related to the LABs' presence [30,32].

The superalloys of the CMSX series are advanced materials commonly used in the aerospace industry for production of SX turbine blades [33]. Currently, the first generation of superalloys including CMSX-6 with a typical dendritic structure, created during directional crystallization, is the best examined. However, so far, the differences in the defect structure created by axial and lateral growth are unknown. This issue is particularly important for modern production methods such as LMC [20]. In the case of the conventional Bridgman process, it is possible to investigate a lateral growth by examining the layers of the root located near the S–R connection of the blades. The relationship between vacancy-type defects and LABs for CMSX-6 alloy has not yet been determined. Additionally, the mechanism for LABs creation in the layers of the root located near the S–R connection is poorly known. Therefore, the main goal of the presented paper is to examine the creation of defects and the relationships between them in the root layers located near the S–R connection, where lateral non-disturbed axial growth occurs.

X-ray diffraction topography is very useful to study the process of creating a dendrites array because it enables the visualization of such small misorientation of the neighboring regions and neighboring dendrites (angular minutes), that cannot be visualized by the other methods (e.g., EBSD). It allows to analyze the creation of defects during the lateral growth of separate dendrites and the creation of the dendrite array.

In the present work, a well-known Cannon–Muskegon 1st generation superalloy—CMSX-6—which does not contain such refractory elements as W and Re was selected for the study. The presented results for CMSX-6 refer to the first part of the study, and in the next part, the CMSX-4 and CMSX-4 Plus superalloys that contain W and Re will be studied, and for which the role of LABs is more significant compared to CMSX-6.

## 2. Materials and Methods

Blades with an axial orientation of the [001] type were obtained by the Bridgman technique using a spiral selector in an industrial ALD furnace at the Research and Development Laboratory for Aerospace Materials at the Rzeszów University of Technology. The withdrawal rate of 3 mm/min was used. The specimens for study were prepared from roots of CMSX-6 turbine blades. For the first step, a fragment T (Figure 1b,c) was cut-off from all blade roots in such a way that the plane  $F$  was parallel to the  $Z$  axis and crossed the fragment of the selector. Mechanical polishing and chemical etching were used for part of the  $F^*$  preparation of the  $F$  surface for SEM observations of the dendrite structure. Then, three slices (A, B, and C) were cut perpendicular to the withdrawal direction  $Z$  near the plane  $M-N$  (Figure 1a,b) of the S–R connection from the remaining root fragment H (Figure 1a). Three plate-shaped specimens, A, B, and C (Figure 1b), were prepared from the slices. The A and B specimens were used to form a sandwich layout for PALS measurements (Figure 1b).

The study procedures comprised the following steps: (1) SEM observations of the dendritic structure on the whole  $P_A-P_A$  and  $P_B-P_B$  surfaces (Figure 1b), (2) analysis of X-ray topograms received from the same surfaces, and (3) examination by PALS of three selected areas of each prepared sandwich. Area 1 of the A and B specimens was chosen because it was representative of the selector extension (SE) area (Figure 1a,b). It was assumed that in the SE area the axial growth of dendrites occurred directly from the selector without any structure disturbances. The other two areas were selected based on the beforehand obtained topograms: area 2 contained one or several macroscopic LABs, and area 3 did not contain such LABs. Additionally, the metallographic section was prepared from the surface  $F^*$  of the T fragment (Figure 1a) for the dendritic structure observation.

The dendritic structure was visualized by macro-SEM images (BSE technique) obtained by stitching several dozen SEM images together using a JEOL JSM-6480 microscope. For X-ray topography, the micro-focus X-ray  $\text{CuK}_\alpha$  source provided by the Panalytical was used. The topograms were

obtained using the 113 type reflections during coupled sample and film oscillation around the Bragg angle. Initially, the samples were crystallographically oriented by the Laue method.

The PALS measurements were performed at room temperature in a sandwich geometry using a “fast–fast” coincidence spectrometer. The positron source with an activity of about 370 kBq covered with a 5- $\mu\text{m}$  Ni foil was used. The data were analyzed using the LT software [34] and were further fitted using the least squares fitting procedure to a simple three-state-trapping model implemented directly to the LT code [34]. This model describes a positron lifetime in the bulk material  $\tau_b$ , two lifetimes of positrons trapped inside two different types of defects  $\tau_1$  and  $\tau_2$ , and two respective positron trapping rates  $\kappa_1$  and  $\kappa_2$ . The values of  $\kappa_1$  and  $\kappa_2$  are proportional to the atomic concentrations of both types of defects. The positrons are trapped in vacancy-type defects (Figure 1d), where the electron density is reduced. It results in a longer positron lifetime in comparison to the bulk. The positron annihilation in the bulk and the defects cause the emission of  $\gamma$  radiation. Measured time intervals between implementation and annihilation of positrons allows to determine their lifetime and the concentration of vacancy-type defects.

### 3. Results and Discussions

In the lateral macro-SEM images of the H-type samples obtained from  $P_A$ – $P_A$  and  $P_B$ – $P_B$  surfaces, two systems of perpendicular secondary dendrite arms parallel to the  $p$  and  $q$  directions were found (Figure 2a). In the  $D_1$  and  $D_2$  areas, marked by white dotted lines, the dendritic structure was finer than in the other part of the sample. In area  $D_1$ , the dendrite arms were arranged in long straight chains (SCs) parallel to  $q$ . A similar distribution of the secondary dendrite arms occurred in the  $D_2$  area, but the SCs were parallel to  $p$  and  $q$ . Some of the longest SCs were indicated as  $L_1$ ,  $L_2$  (parallel to  $q$ ), and  $L_3$  (parallel to  $p$ ) in Figure 2a. In the middle part of the specimen, corresponding to the SE area (circular area, Figure 2a), the SCs occurred much less frequently. The SCs were also present around the SE area.

Figure 2b presents an example of an X-ray topogram obtained for the  $P_A$ – $P_A$  surface. The topogram of the  $P_B$ – $P_B$  surface was similar. Three sub-grains were visible:  $SG_A$ ,  $SG_B$ , and  $SG_C$  (Figure 2c,b), separated by wide contrast bands of BI and BII with decreased contrast. The bands corresponded to the macroscopic LABs, LAB-I and LAB-II, respectively. Such LABs are characteristic for Ni-based superalloys [9,16,18]. Additionally, in the topogram, groups of long bands of increased and decreased contrast were visible. They are marked by  $L'_1$ – $L'_3$  in Figure 2b,d and by  $L'_4$ – $L'_7$  in Figure 2d ( $L'_4$ – $L'_7$  were not marked in Figure 2b to increase the clarity of the topogram). Moreover, the circular area without long bands in the region corresponding to the SE area may be observed. The bands on the topograms were parallel to the  $p'$  and  $q'$  directions, which were parallel to [010] and [100] directions defined by the Laue diffraction. These bands corresponded to the  $p$  and  $q$  directions of the secondary dendrite arms (Figure 2a), although the  $p'$  and  $q'$  directions were not perpendicular to each other in the topogram. Additionally, the contour of the topogram was slightly different than the outline of the macro-SEM image, consistent with the shape of the sample. The difference results from the fact that the diffraction planes of the (113) type used for topograms were not parallel to the surface tested by SEM. The angle between the surface of the samples and the planes of the (113) type was  $\beta = 20^\circ$  (Figure 2e). Neighboring bands of low- and high-contrast intensity, such as  $S_1$  and  $S_2$  (Figure 2d), were created as a result of the bands' shift in the topograms (Figure 2e). Such a shift indicates a crystal misorientation of neighboring sample areas, and bands with this shift are interpreted as a macroscopic LAB-like, because they have a different character than LAB-I and LAB-II. When comparing such bands ( $L'_1$ – $L'_3$  in Figure 2b or  $L'_4$ – $L'_7$  in Figure 2d) with the macro-SEM image it can be observed that they were formed in the SCs regions of the dendritic structure. It means that when the secondary arms form the SC it causes the misorientation of the entire chain in relation to the neighboring part of the dendritic structure. In the SE part, this effect does not occur or is much weaker.

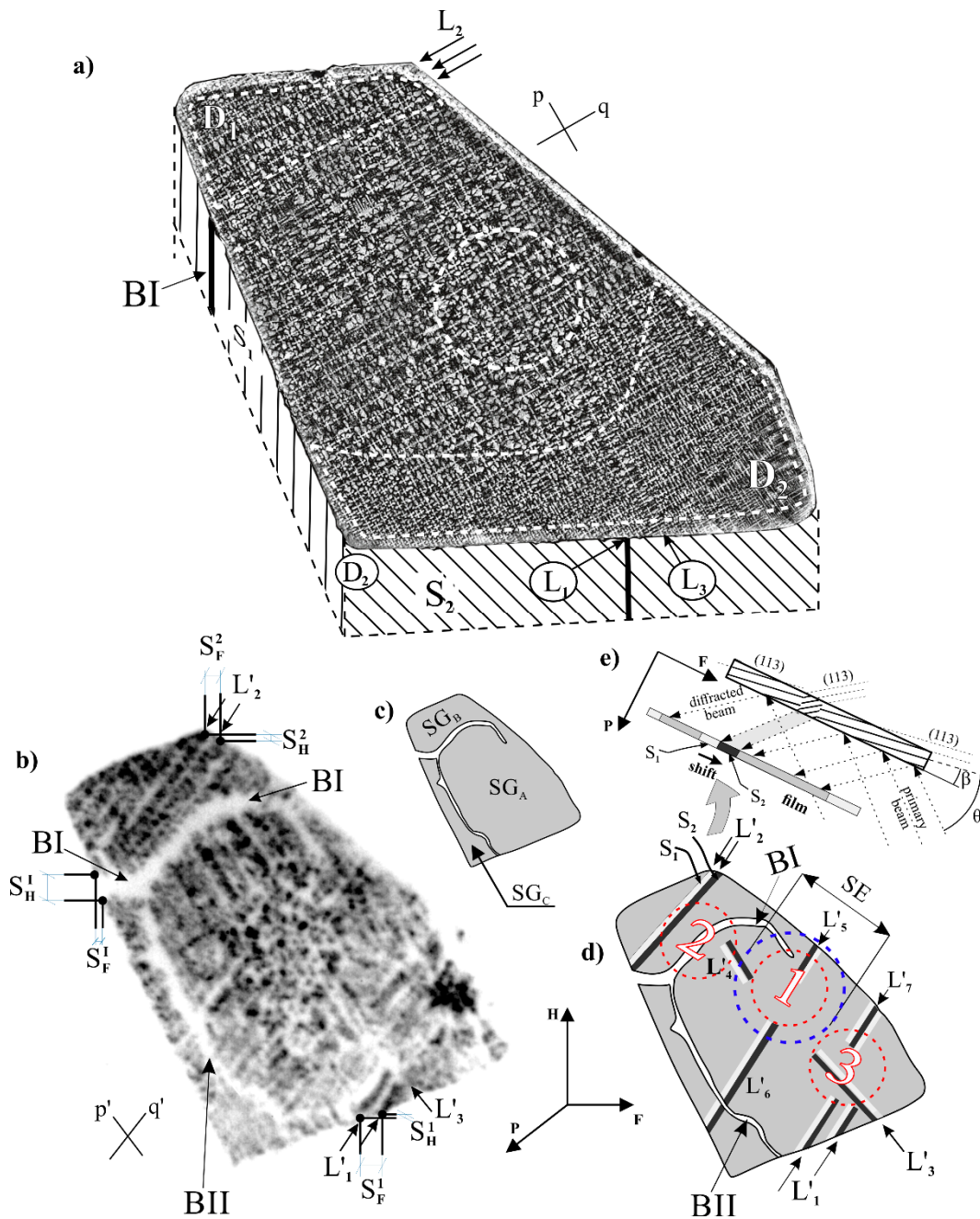


**Figure 2.** (a) Example of a macro-SEM image obtained from the  $P_A$ - $P_A$  surface;  $p$  and  $q$ —the directions of dendritic arms; (b) example of the topogram obtained from the  $P_A$ - $P_A$  surface; BI, BII—the contrast bands visualize the macroscopic low-angle boundaries LAB-I and LAB-II;  $p'$  and  $q'$ —the directions of the contrast bands in the topogram; axis H and F lie in the plane of the microsection and the P axis is perpendicular to them; (c) scheme of sub-grains  $SG_A$ ,  $SG_B$ , and  $SG_C$  visualized in the topogram; (d) scheme of the topogram with marked areas 1, 2, and 3 for PALS measurements; SE—selector extension area of root; (e) scheme of the contrast bands formation in the topogram.

It should be emphasized that on the basis of the macro-SEM images only, it is difficult or not possible to identify the LABs or LAB-like type and SE type area. However, the location and shape of possible disturbances in the dendritic structure may be indicated in the topograms [18].

Based on the topogram presented in Figure 2b, the components  $\varphi_F$  and  $\varphi_H$  of misorientation angles for the LAB-I and LAB-like  $L_1$  were calculated using the Formulas (1) and (2) [35]:

$$\sin \varphi_F = \frac{1}{2 \sin \theta_{113}} \cdot \frac{S_H}{\sqrt{S_H^2 + R^2}} \quad (1)$$

$$\sin \frac{\varphi_H}{2} = \frac{S_F}{2R} \cdot \sin(\theta_{113} - \beta), \quad (2)$$

where  $S_H$  and  $S_F$  are the shifts along the H and F axes measured in the topogram,  $\theta_{113}$  is the Bragg angle equal to  $47^\circ$ ,  $\beta$  is the angle between the surface of the samples and diffraction planes equal to  $20^\circ$  (Figure 2e), and  $R$  is the sample film distance equal to 78 mm. The total misorientation angle for LAB-I and LAB-like  $L_1$  was calculated based on Formula (3):

$$\varphi = \sqrt{\varphi_H^2 + \varphi_F^2 + \varphi_P^2} \quad (3)$$

where component  $\varphi_P$  was calculated based on the additional topograms obtained from the surfaces  $S_1$  and  $S_2$  (Figure 2a). The calculated values of  $\varphi_I$  for LAB-I and  $\varphi_{L1}$  for LAB-like  $L_1$  were  $1.05^\circ$  and  $0.64^\circ$ . The misorientation value of LAB-like  $L_1$  will be further marked as  $\varphi_L$ , which is characteristic for LAB-like.

The PALS analysis was performed in areas 1, 2, and 3 (Figure 2d) with the use of positron lifetime  $\tau_b$  in bulk material as a common parameter. The determined value of  $\tau_b$  was  $130 \pm 1$  ps. This value was a bit higher than the theoretical (110 ps [36,37]) and experimental values for  $\text{Ni}_3\text{Al}$  (112 ps [38] and 125 ps [39]). The differences were related to large amounts of CMSX-6 alloying elements, e.g., Cr, Co, Mo, Ti, Ta, and Hf [33]. The fitting of the simple three-state trapping model allowed to determine the positron trapping rates  $\kappa_1$  and  $\kappa_2$  for each area from 1 to 3. The values of  $\kappa$  were used for estimation of vacancy concentration ( $c_V$ ) based on the equation  $c_V = \kappa/\mu$ . In these calculations, it was assumed that the positron trapping coefficient ( $\mu$ ) did not depend on the local environment of vacancy and was  $2.5 \times 10^{14} \text{ s}^{-1}$  [38]. The essential results of the PALS analysis are shown in Figure 3. Based on the theoretical results and obtained values, it was found that  $\tau_1$  and  $\tau_2$  corresponded to annihilation lifetime in mono-vacancies and in vacancy clusters, respectively, with the nickel vacancy behavior.

The obtained values of positron lifetimes (178 ps) indicated that in area 1 (Figure 3), only mono-vacancies in the  $\gamma'$  phase were present. It can be assumed that the high structure homogeneity was the result of undisturbed axial growth of the primary dendrites from the selector toward the inside of the SE area. In areas 2 and 3, two types of defects were identified. Apart from the mono-vacancies in the  $\gamma'$  phase, vacancy clusters were also found. The area containing LABs of type I (area 2) had a higher mono-vacancies concentration (Figure 3, marked as hatched bars) in comparison to the areas without LABs similar to LAB-I (area 3).

The PALS results show that the concentration of the vacancy clusters (Figure 3, marked as cross-hatched bars) was also higher in area 2 compared to area 3. However, the values of the positron lifetime in area 3 ( $\tau_1 = 185$  ps,  $\tau_2 = 197$  ps) were similar as in area 2 ( $\tau_1 = 183$  ps,  $\tau_2 = 209$  ps), which were related to the presence of mono-vacancies and vacancy clusters in both areas. The slight different positron lifetime values were probably related to the differences in the local environment of vacancy-type defects. The differences may be also related to the different local crystal misorientation in areas 2 and 3. Additionally, for area 2, it can also be related to the presence of LAB-I-type (Figure 2b–d), composed of a net of dislocations with increased concentration. It may cause an increase in the vacancy concentration, because  $\varphi_I > \varphi_L$  suggests a higher dislocation density.

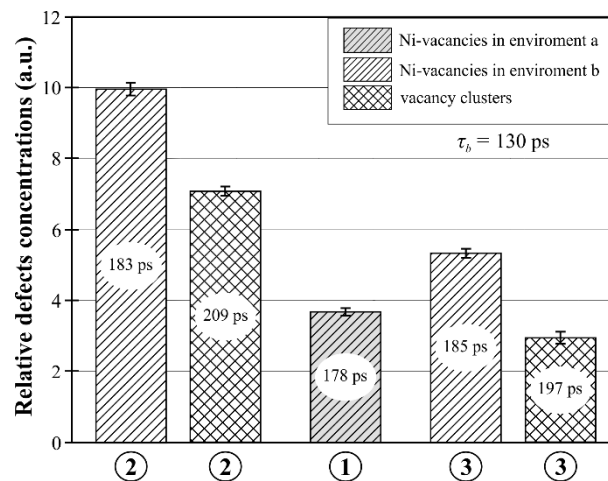


**Figure 3.** The relative concentration of different types of defects in areas 1, 2, and 3 with error bars and the values of positron lifetime.

The positron lifetime that corresponded to dislocations was not found for any of the three areas. It confirms the assumption that the annihilation rate for the vacancy-type defects was higher than for the dislocations, and all positrons emitted from the source were quickly trapped and annihilated on vacancy-type defects but not on dislocations. The mono-vacancy concentration determined by the PALS method applied to both equilibrium vacancies and non-equilibrium vacancies. Non-equilibrium vacancies may be related to the heterogeneity of chemical composition and occurrence of pores or dislocations [31]. The differences in the concentration of mono-vacancies in areas 1, 2, and 3 were related to the change of non-equilibrium defects only, assuming that in the macroscopic areas of 1, 2, and 3, where the positron source was active, the average macroscopic chemical composition and temperature were the same. The clusters of vacancy were non-equilibrium defects, so the values and changes of the concentration in areas 2 and 3 were directly defined by PALS.

The topogram presented in Figure 2b was formed by contrast related to the crystal orientation. Therefore, different details in the topograms were related to different distributions and values of local crystal orientation. Based on the generally accepted assumptions that all dendrite arms grow exactly in the  $\langle 001 \rangle$  type direction, it may be concluded that topograms visualize the local change of the dendrites' growth directions. Analysis of the topograms shows that the bands of misoriented areas type  $L'_1-L'_7$ , (Figure 2b,d) occurred outside the SE area, e.g., in areas 2 and 3 of the PALS measurement. The areas of the PALS sandwich (Figure 1b) were located in specimens A and B, placed above specimen C, inside which the unsteady lateral growth of the secondary dendrite arms in directions L (Figure 1b) may appear. The lateral growth occurs in the layer located directly above plane of S–R connection and may affect the creation of the dendrite array in the specimens A and B. Therefore, the microstructure of specimen section  $F^*$  (Figure 1a) were studied in detail.

Figure 4a shows the dendritic structure visualized on the surface  $F^*$  of the  $F$  section. Figure 4b shows the scheme of the array of dendrite arms that were roughly parallel to the axis Y. The scheme was prepared by creation of skeletal images and modification of contrast. Skeletonization is a technique whereby a binary image of dendrites is eroded away step by step, until the skeleton of the image is obtained. The skeletal image is created as a thin line equidistant from the original edges of the binary dendrites' shape [18].

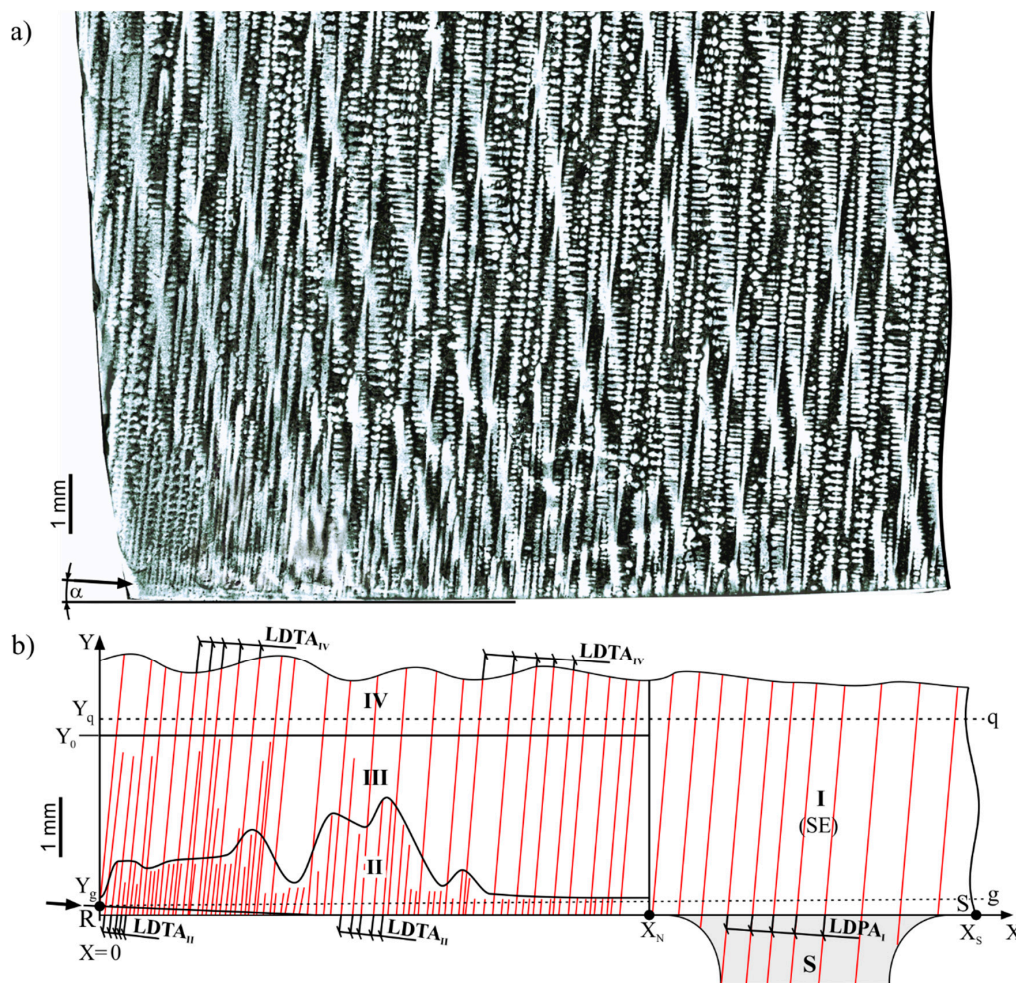


**Figure 4.** (a) The dendritic structure visualized on the surface  $F^*$  of the root part T; (b) the dendritic array scheme with growth areas marked as I, II, III, and IV.

The surface  $F^*$  of the  $F$  section (Figure 4b) may be divided into four areas corresponding to different morphologies of the dendrite array: I, II, III, and IV, and which may be named as growth areas. Additionally, the  $q$  and  $g$  lines were marked. The line  $q$  crossed the area I and IV at the level of  $Y_q$ . The line  $g$  crossed the area I and II at the level  $Y_g$ . The area I was a fragment of SE (Figure 4b), where the primary arms grew directly from the selector without structural disturbances. The distance between the primary dendrite arms visualized in area I is denoted as the linear distance of the primary arms ( $LDPA_I$ ) unlike the primary arm spacing (PAS), determined usually in the transverse section [20]. The dendritic growth roughly along the  $y$ -axis in areas II, III, and IV was followed by tertiary arms, growing from some secondary arms of area II, marked by arrows in the left side of Figure 4a,b. The distance between tertiary dendrite arms in areas II, III, and IV is denoted as the linear distance of tertiary arms ( $LDTA_{II}$ ,  $LDTA_{III}$ , and  $LDTA_{IV}$ , respectively). These distances and  $LDPA_I$  were measured between the axis of the neighboring arms along the line perpendicular to the primary and tertiary dendrite arms. The  $LDPA_I$  and  $LDTA_{IV}$  refer to the primary and tertiary dendrite arm spacing (PAS and TAS). The PAS and TAS values were determined by classical method with standard deviation in the microstructure of the transverse section of the T fragment of the roots (Figure 1a). It was measured that  $PAS = 502 \pm 92 \mu\text{m}$  and  $TAS = 355 \pm 70 \mu\text{m}$ . The RS segment in Figure 4b corresponds to the segment RS at the bottom root surface (Figure 1a,c). In growth area I, the  $LDPA_I$  values were similar and amount to an average of  $515 \pm 90 \mu\text{m}$ . Growth area II, with a thickness that fluctuated from 0.5 to 2 mm, was located between  $X = 0$  and  $X = X_N$  (Figure 4b). The  $LDTA_{II}$  value in the area II was constant along the  $y$ -axis and gradually increased along the  $x$ -axis. In Figure 4b, above growth area II,

there was growth area III with high changes in  $LDTA_{III}$ . In the left fragment of growth area III, the  $LDTA_{III}$  value increased stochastically in the direction of the  $y$ -axis in such a way that near  $Y = Y_0$ , the  $LDTA_{III}$  became constant and equal to  $LDTA_{IV}$ . In the right fragment of growth area III, the  $LDTA_{III}$  was approximately constant and equal to  $LDTA_{IV}$ . In the fragment of line  $q$  (from  $X = 0$  to  $X = X_N$ ), the  $LDTA_{IV}$  was close to the  $LDTA_I$  and amounted to  $490 \pm 90 \mu\text{m}$ . This means that the average linear distance of primary (growth area I) and tertiary (growth area IV) dendrite arms were similar from  $X = 0$  to  $X = X_S$  in the  $q$  line (Figure 4b).

The relationship between the linear distance of the primary and tertiary arms denoted, as LDA and the  $X$  values along the  $g$  and  $q$  lines marked as  $LDA_g(x)$  and  $LDA_q(x)$ , as well as hypothetical shape of the crystallization fronts, are presented in Figure 5. Lines visible in Figure 5 are the trend lines.

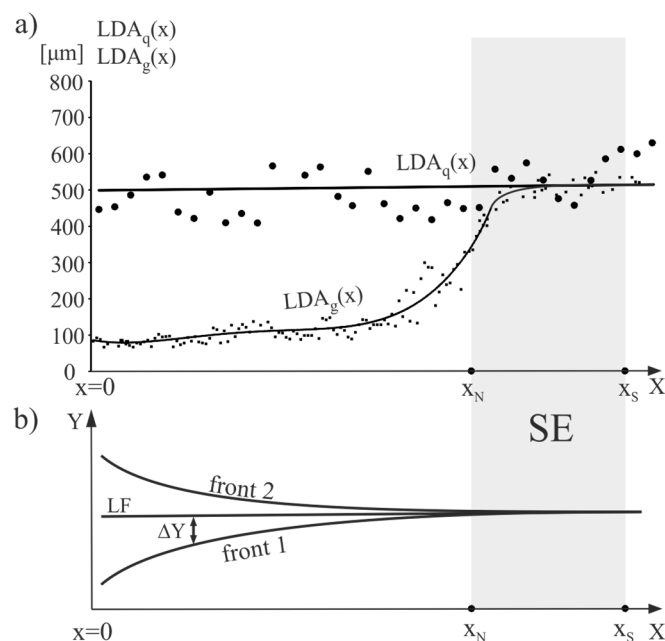


**Figure 5.** (a) The  $LDA_g(x)$  and  $LDA_q(x)$  relations; (b) hypothetical shape of crystallization fronts. LF—linear front perpendicular to the withdrawal direction.

It can be seen that the  $LDA_q(x)$  was approximately constant and the  $LDA_g(x)$  increased from  $x = 0$  to  $X = X_N$ , reaching the value of the  $LDA_q$  in the vicinity of  $X_N$ . The above dendritic array creation and character of the  $LDA_g(x)$  and  $LDA_q(x)$  relations can be described as follows. Growth area II was a layer in which lateral growth occurred under non-steady-state conditions. A selected secondary dendrite arm (arrow in Figure 4a,b) inclined at a small angle  $\alpha$  of about  $6^\circ$  in relation to the  $x$ -axis, grew rapidly from the SE area. Fine tertiary dendrite arms grew from this arm approximately along  $y$ -axis. The growth rate of the secondary arms and tertiary arms in growth area II was much higher than the growth rate of the primary arms in growth area I, which was revealed by a much lower  $LDTA$  value about  $100 \mu\text{m}$  (Figure 5a). In transition growth area III, some of the tertiary dendrite arms ceased to grow as a result of competitive growth process, and the  $LDTA$  increased to reach the value of the  $LDTA_{IV}$  in growth area IV. In this area, the dendrites' growth took place already in steady-state conditions, corresponding to the withdrawal rate of  $3 \text{ mm/min}$ , as in growth area I (SE) of undisturbed growth. The secondary dendrite arm marked in Figure 4a by the arrow may be named the leading arm. These type of dendrite arms create the chains of tertiary arms, which after steadying conditions, form the SCs coming from the SE (e.g.,  $L_3$ ), visible in the transverse microsection and topogram (Figure 2a,b). If it is assumed that the crystallization front moves in the direction  $Y$  at  $3 \text{ mm/min}$ , the rate of axial growth is  $V_{ax} \approx 3 \text{ mm/min}$ . (Figure 6). With the additional assumption that the crystallization front is

perpendicular to  $V_{ax}$  and is flat from  $X = 0$  to  $X = X_S$ , the lateral growth rate  $V_L$  of the leading secondary dendrite arm can be related to  $V_{ax}$  and expressed by the formula:

$$V_{Le} = V_{ax} / \sin \alpha, \quad (4)$$

where  $\alpha$  is an inclination angle of the leading arm. For example, if  $\alpha = 6^\circ$  then  $\sin 6^\circ \approx 0.1$ , therefore, the  $V_L$  is one order of magnitude higher than  $V_{ax}$ . However, when the distance from the SE is higher (i.e., at  $X \rightarrow 0$ ), the fragments of the crystallization front do not keep up with the movement of the front towards  $V_{ax}$  (Figure 5b) in the SE area, and a convex bending of the solidification front is created (front 1, Figure 5b). The local delay of the crystallization front fragments is described by the  $\Delta Y$  value in Figure 5b. The value of  $\Delta Y$  increases when approaching  $X = 0$ . If  $\Delta Y$  increases, the local undercooling  $\Delta T$  must increase and the LDTA decrease (Figure 5a). A similar mechanism is presented in Reference [20]. On the other hand, the lateral heat dissipation can cause concave bending of the solidification front (front 2, Figure 5b) [7,20,40,41]. There is an accumulation of the abovementioned effects for growth area II resulting in formation of real crystallization front shape.

The  $L'_1$ – $L'_7$  bands in the topogram are parallel to the SCs, while LAB-I and LAB-II have another arrangement. They are located near the side walls of the root and are almost parallel to these walls. These types of LABs may be a result of the concave curvature of isotherm [6,7], solid–liquid interface, and crystallization front.

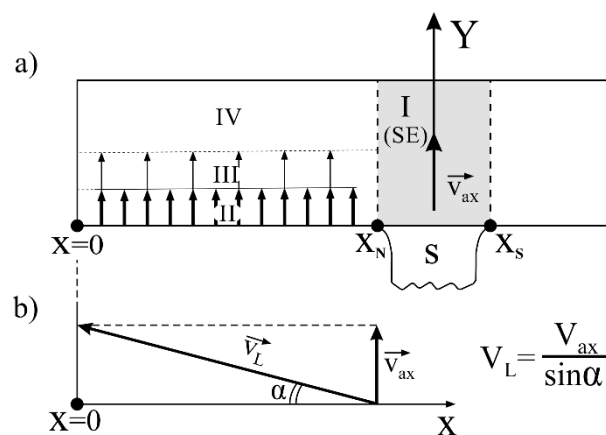


**Figure 6.** (a) Scheme of axial growth of dendrites in growth areas I–IV presented in Figure 4; (b) scheme that illustrates the relation between axial- $V_{ax}$  and lateral- $V_L$  rates of dendrite growth in area II. The  $\alpha$  angle and thickness of growth area II are increased for figure clarity. Y—the direction of the crystallization front movement.

The rate of lateral growth in growth area II in unsteady-state conditions was much higher than axial growth of the primary arms in the SE region. This is the reason for the crystal misorientation of the dendrites in SCs originating from the leading secondary dendrite arm in growth area II. These misorientation defects were inherited by the areas of the root which crystallized later in steady-state conditions. This inheritance takes place through the growth of the tertiary dendrite arms after finishing the competitive growth process in transition area III. Therefore, it can be concluded that the formation of SCs are the reason for the LAB-like creations. Inside the SE region, the SCs did not occur or occurred rarely.

The differences in the values of the misorientation angle of LABs and LAB-like defects, as well as the differences in array and morphology of the dendrites are related to changes in concentration and type of vacancy defects. On the one hand, only mono-vacancies were present in the SE areas, and on the other, the mono-vacancies with the vacancy clusters were present in the areas with bands of crystal misorientation, visible as the SCs (area 3, Figure 2c). This means that the vacancy clusters were related to the crystal misorientation of the secondary arms in the SCs. In area 2 of the PALS

measurements, the concentration of vacancy clusters and mono-vacancies was higher when compared to area 3. There were misoriented contrast bands in area 3 originating only from the SCs, similar to area 2, where the LAB-I, with a much higher misorientation angle, was additionally present.

The formation of vacancy clusters in areas containing low-angle boundaries (e.g., area 2 of PALS measurement, Figure 2d) was a complicated process that may be based on two basic phenomena: diffusion of vacancies to dislocations and the Kirkendall effect in  $\gamma$  phase, mainly at temperatures above the solvus, as what was described for nickel-based superalloys in Reference [42]. The low-angle boundaries created by locked-dislocation systems cause diffusion of vacancies toward them (Figure 7a). As a result, the mono-vacancy accumulation occurs at the LABs. It should be noted that during solidification, the alloying elements are segregated in the diffusion area of liquids, in such a way that the majority of the high-melting elements of Co, Mo, and Cr diffuse into dendrites, and the low-melting elements of Al and Ti into the inter-dendritic regions. Between these regions of the  $\gamma$  phase (above the solvus temperature), a gradient of the concentration of elements was formed. In the further crystallization step, the  $\gamma \rightarrow \gamma'$  transition takes place in the solid phase. The concentration gradient causes the high melting elements Co, Mo, and Cr to diffuse from the dendrite into the inter-dendritic region, and the elements with a lower melting point, such as Al and Ti, go in the opposite direction. Since there are different diffusion coefficients for both types of elements, according to Kirkendall's theory, the vacancies were created by a diffusion mechanism. In the inter-dendritic region, additional vacancies appeared (light elements have a higher diffusion coefficient and leave their positions faster than they are planted by Co, Cr, and Mo). Created vacancies diffuse also to low-angle boundaries, where they accumulate, and their concentration becomes so high that it is sufficient to form clusters. Moreover, because vacancy clusters appear mainly through heterogeneous nucleation, a probability of the concentration in LABs was higher [43].

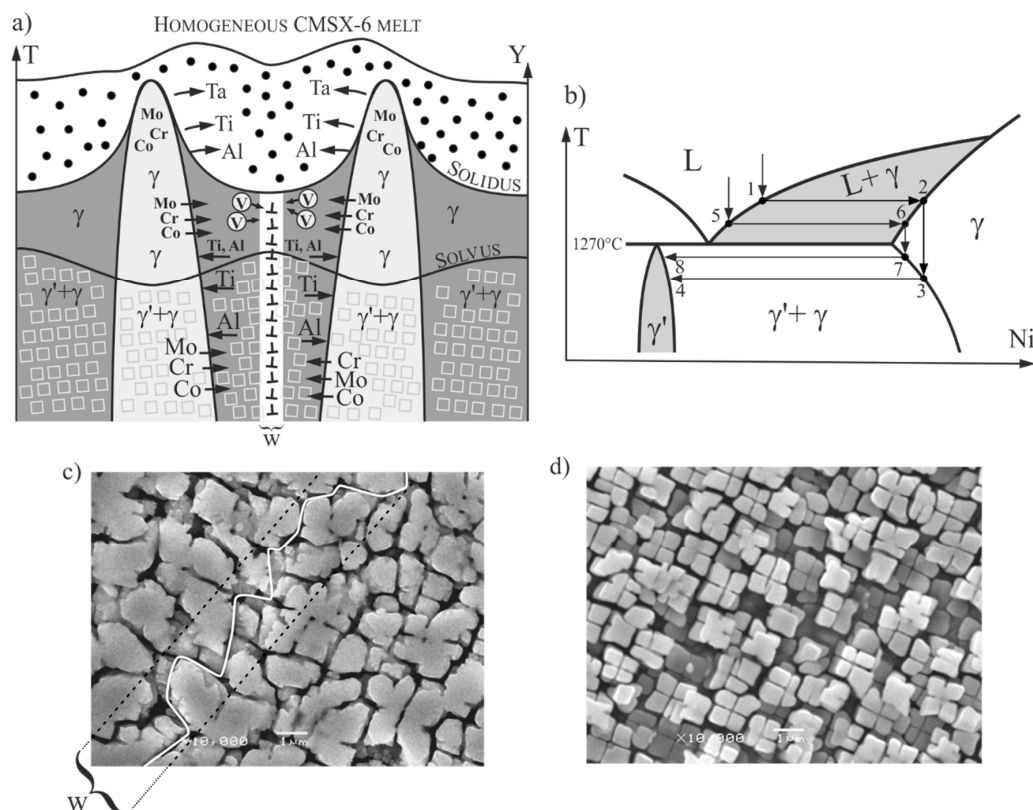


**Figure 7.** (a) Scheme of alloying elements' distribution in the LAB area; (b) fragment of Ni–Al phase diagram; (c) example of  $\gamma/\gamma'$  structure typical for areas 1, 2, and 3 of the PALS measurements in inter-dendritic regions and (d) in dendritic regions. Dotted area—diffusion area of liquid, W—the hypothetical LAB area, V—vacancies.

The creation of vacancy clusters in superalloys with a lot of alloying elements can be done through other, more complex mechanisms, related to the alloying elements' interactions and preferences in occupancy of the lattice node. In area 1 of the PALS measurements (Figure 2d), vacancy clusters were not created because there was no LAB and LAB-like defects, and the concentration of vacancies was not yet reached, allowing for the creation of clusters. In area 2 (Figure 2d), the density of vacancies and clusters was higher than in area 3, because the LAB in area 2 had a larger misorientation angle and higher dislocation density.

The vacancies of the  $\gamma'$  phase identified by PALS in areas 2 and 3 (Figure 2d) were formed mainly in the  $\gamma$  phase at high temperatures above the  $\gamma \rightarrow \gamma'$  transition. Let us consider the process of vacancies inheritance from  $\gamma$  to  $\gamma'$  phase. The processes of diffusion of vacancies to dislocations and the Kirkendall effect described above, take place mainly in the  $\gamma$  phase below the solidus and above the solvus temperature. Creation of  $\gamma/\gamma'$  structures are described for dendrites by paths marked on fragments of the equilibrium Al–Ni diagram (Figure 7b) through points 1–4, and for inter-dendritic regions through points 5–8. The diagram shows that the temperature difference between points 2 and 3 is higher than between points 6 and 7. This means that in the inter-dendritic regions, the difference between the temperature of the solidus and solvus was lower (Figure 7a), which is related to the shorter time between the beginning of the creation of vacancies and the beginning of transformation  $\gamma \rightarrow \gamma + \gamma'$ . It follows that the vacancies created and collected in the  $\gamma$  phase near LAB will only partially relax before the transformation  $\gamma \rightarrow \gamma + \gamma'$ . This means that higher quantities of vacancies will be inherited by the  $\gamma'$  phase near the LAB.

The dislocations density in area 2 and 3 (Figure 2d) can be calculated based on the values of misorientation angles of LABs and LAB-like defects. It can be assumed that for Ni-based superalloys, the LABs passed through the  $\gamma$  phase between  $\gamma'$  precipitates in the area indicated, for example as  $W$  (Figure 7c) which had a value of about 2.5  $\mu\text{m}$ . The assumption may be based on the fact that LABs are created in the  $\gamma$  phase, before the  $\gamma'$  formation. The broken line of the LAB (Figure 7c) suggests the occurrence of both edge and screw dislocations in the LABs. The spacing of dislocations, separate for edge and screw type, can be expressed by Equations (5) and (6), respectively:

$$D_e = |\vec{b}| / \sin \varphi, \quad (5)$$

$$D_s = |\vec{b}| / 2 \sin \varphi, \quad (6)$$

where  $\varphi$  is the LABs or LAB-like misorientation angle and  $b$  is the Burgers vector. The Burgers vector for  $\gamma$  phase is  $|\vec{b}| = a\sqrt{2}/2$ , where  $a$  is the lattice parameter. The dislocations density may be determined for macroscopic LABs and LAB-like defects. Taking into account the  $W$  value, the edge and screw dislocations density for macroscopic LABs may be expressed by Equations (7) and (8), respectively:

$$\rho_{me} = \frac{1}{D_e \cdot W} \quad (7)$$

$$\rho_{ms} = \frac{1}{D_s \cdot W} \quad (8)$$

The edge dislocations density calculated for the LAB-I in area 2 of the PALS measurement (Figure 2d) was  $\rho_{me2} = 3 \times 10^{10} \times 1/\text{cm}^2$  and the screw dislocations density was  $\rho_{ms2} = 6 \times 10^{10} \times 1/\text{cm}^2$ . In addition to the macroscopic LABs, there were micro-LABs located between misoriented neighboring dendrites [44]. Taking into account the TAS value, the edge and screw dislocations density for micro-LABs may be expressed by the relations, similar to that presented in Reference [44]:

$$\rho_{\mu e} = \frac{1}{D_e \cdot \text{TAS}} \quad (9)$$

$$\rho_{\mu s} = \frac{1}{D_s \cdot T A S} \quad (10)$$

The edge dislocations density calculated for micro-LABs in area 2 was  $\rho_{\mu e2} = 2 \times 10^7 \times 1/\text{cm}^2$  and the screw dislocations density was  $\rho_{\mu s2} = 4 \times 10^7 \times 1/\text{cm}^2$ . The edge dislocations density calculated for micro-LABs in area 3 was  $\rho_{\mu e3} = 1 \times 10^7 \times 1/\text{cm}^2$  and the screw dislocations density was  $\rho_{\mu s3} = 2 \times 10^7 \times 1/\text{cm}^2$ . The abovementioned values are similar to the ones presented in Reference [44].

Except the macroscopic low-angle boundaries of the LAB-I and LAB-like type defects revealed by X-ray topography, in areas 1, 2, and 3 of the PALS measurements, there were micro-LABs located between neighboring misoriented dendrites. The micro-LABs were difficult to reveal using X-ray topography with conventional X-ray source, but such micro-LABs may be visualized and the misorientation angle may be determined using synchrotron radiation [44]. However, based on the PALS results, in area 1 with a lack of LAB-I-type and LAB-like defects, the presence of mono-vacancies suggest that they may be related to the abovementioned micro-LABs. Therefore, a comprehensive defect analysis was possible only with the use of different methods with different sensitivities to defects of various size scales.

#### 4. Conclusions

1. Two types of macroscopic defects of misorientation character were formed outside the selector extension (SE) area. The first type of the LAB-like misorientation defects with misorientation angle of about  $0.6^\circ$  was formed by the lateral growth of some secondary dendrite arms near the surface of the selector–root connection. The second type were the LABs with higher misorientation angles of about  $1^\circ$  that were created in the periphery of the root transverse section. In the SE area of the root, the macroscopic defects of the low-angle boundaries (LABs) type were not formed. It was related to undisturbed axial growth of primary dendrite arms directly from the selector.
2. It was found that in the SE area of the root, only Ni mono-vacancies occurred. There were two types of point defects in the root part, outside the SE area: Ni mono-vacancies with a predominant concentration, and the vacancy clusters. In addition, the local environment of the defects in atomic scale was different in these areas. The vacancy clusters occurred in the areas where macroscopic LABs and LAB-like defects were present as opposed to the SE area. It can be concluded that the vacancy clusters were related to LABs and LAB-like defects. Additionally, the areas with the LABs of higher misorientation angles than LAB-like defects differed in higher concentrations of the mono-vacancies and the vacancy clusters. It may be related to the increased dislocation density of the LABs.
3. A combination of X-ray diffraction topography and positron annihilation lifetime spectroscopy allowed to determine the relation between the LAB-type defects and the vacancy-type defects created in the root areas of CMSX-6 single-crystalline as-cast blades.

**Author Contributions:** Conceptualization, W.B. and J.K.; methodology, W.B. and J.K.; software, A.H.-K.; investigation, R.P. and B.T.; data curation, A.H.-K., R.P., W.B. and J.K.; writing—original draft preparation, W.B. and J.K.; writing—review and editing, W.B. and J.K.; visualization, R.P., J.K. and W.B.; supervision, J.S.; project administration, J.S.

**Funding:** This research received no external funding.

**Conflicts of Interest:** The authors declare no conflict of interest.

#### References

1. Warnken, N. Studies on the solidification path of single crystal superalloys. *J. Phase Equilib. Diffus.* **2016**, *37*, 100–107. [[CrossRef](#)]
2. Beckermann, C.; Gu, J.P.; Boettinger, W.J. Development of a freckle predictor via rayleigh number method for single-crystal nickel-base superalloy castings. *Met. Mater. Trans. A* **2000**, *31*, 2545–2557. [[CrossRef](#)]

3. Qin, L.; Shen, J.; Li, Q.; Shang, Z. Effects of convection patterns on freckle formation of directionally solidified Nickel-based superalloy casting with abruptly varying cross-sections. *J. Cryst. Growth* **2017**, *466*, 45–55. [[CrossRef](#)]
4. Napolitano, R.E.; Schaefer, R.J. The convergence-fault mechanism for low-angle boundary formation in single-crystal castings. *J. Mater. Sci.* **2000**, *35*, 1641–1659. [[CrossRef](#)]
5. Yang, X.L.; Dong, H.B.; Wang, W.; Lee, P.D. Microscale simulation of stray grain formation in investment cast turbine blades. *Mater. Sci. Eng. A* **2004**, *386*, 129–139. [[CrossRef](#)]
6. Wang, W.; Kermanpur, A.; Lee, P.D.; Mclean, M. Simulation of dendritic growth in the platform region of single crystal superalloy turbine blades. *J. Mater. Sci.* **2003**, *38*, 4385–4391. [[CrossRef](#)]
7. Szeliga, D.; Kubiak, K.; Sieniawski, J. Control of liquidus isotherm shape during solidification of Ni-based superalloy of single crystal platforms. *J. Mater. Process. Technol.* **2016**, *234*, 18–26. [[CrossRef](#)]
8. Billia, B.; Bergeon, N.; Nguyen Thi, H.; Jamgotchian, H. Cumulative mechanical moments and microstructure deformation induced by growth shape in columnar solidification. *Phys. Rev. Lett.* **2004**, *93*, 126105. [[CrossRef](#)]
9. Bogdanowicz, W.; Tondos, A.; Krawczyk, J.; Albrecht, R.; Sieniawski, J. Dendrite growth in selector-root area of single crystal CMSX-4 turbine blades. *Acta Phys. Pol. A* **2016**, *130*, 1107–1109. [[CrossRef](#)]
10. D'Souza, N.; Newell, M.; Devendra, K.; Jennings, P.A.; Ardakani, M.G.; Shollock, B.A. Formation of low angle boundaries in Ni-based superalloys. *Mater. Sci. Eng. A* **2005**, *567*, 413–414. [[CrossRef](#)]
11. Miller, J.D.; Yuan, L.; Lee, P.D.; Pollock, T.M. Simulation of diffusion-limited lateral growth of dendrites during solidification via liquid metal cooling. *Acta Mater.* **2014**, *69*, 47–59. [[CrossRef](#)]
12. Hong, J.; Ma, D.; Wang, J.; Wang, F.; Sun, B.; Dong, A.; Li, F.; Bührig-Polaczek, A. Freckle defect formation near the casting interfaces of directionally solidified superalloys. *Materials* **2016**, *9*, 929. [[CrossRef](#)] [[PubMed](#)]
13. Meyer ter Vehn, M.; Dedecke, D.; Paul, U.; Sahm, P.R. Undercooling related casting defects in single crystal turbine blades. In *Superalloys 1996*; Kissinger, R.D., Deye, D.J., Anton, D.L., Cetel, A.D., Nathal, M.V., Pollock, T.M., Woodford, D.A., Eds.; TMS: Warrendale, PA, USA, 1996; pp. 471–479.
14. Ma, D.; Wang, F.; Wu, Q.; Bogner, S.; Bührig-Polaczek, A. Innovations in casting techniques for single crystal turbine blades of superalloys. In *Superalloys 2016*; Hardy, M.C., Huron, E.S., Glatzel, U., Griffin, B., Lewis, B., Rae, C., Seetharaman, V., Tin, S., Eds.; TMS: Warrendale, PA, USA, 2016; pp. 237–246.
15. Bogdanowicz, W.; Albrecht, R.; Sieniawski, J.; Kubiak, K. The subgrain structure in turbine blade roots of CMSX-4 superalloy. *J. Cryst. Growth* **2014**, *401*, 418–422. [[CrossRef](#)]
16. Bogdanowicz, W.; Krawczyk, J.; Tondos, A.; Sieniawski, J. Subgrain boundaries in single crystal blade airfoil of aircraft engine. *Cryst. Res. Technol.* **2017**, *52*, 1600372. [[CrossRef](#)]
17. Krawczyk, J.; Tondos, A.; Bogdanowicz, W.; Paszkowski, R. Structural defects of initial crystallization areas in single-crystalline turbine blades. *Powder Metall. Met. Ceram.* **2017**, *56*, 481–486. [[CrossRef](#)]
18. Krawczyk, J.; Bogdanowicz, W.; Hanc-Kuczkowska, A.; Tondos, A.; Sieniawski, J. Influence of heat treatment on defect structures in single-crystalline blade roots studied by X-ray topography and positron annihilation lifetime spectroscopy. *Met. Mater. Trans. A* **2018**, *49*, 4353–4361. [[CrossRef](#)]
19. Schenk, T.; Trehorel, R.; Dirand, L.; Jacques, A. Dislocation Densities and Velocities within the  $\gamma$  Channels of an SX Superalloy during In Situ High-Temperature Creep Tests. *Materials* **2018**, *11*, 1527. [[CrossRef](#)] [[PubMed](#)]
20. Miller, J.D. Heat Extraction and Dendritic Growth during Directional Solidification of Single-Crystal Nickel-Base Superalloys. Ph.D. Dissertation, University of Michigan, Ann Arbor, MI, USA, 2011.
21. Segersäll, M.; Moverare, J.J. Crystallographic Orientation Influence on the Serrated Yielding Behavior of a Single-Crystal Superalloy. *Materials* **2013**, *6*, 437. [[CrossRef](#)] [[PubMed](#)]
22. Bowen, D.K.; Tanner, B.K. *High Resolution X-ray Diffractometry and Topography*; CRC Press: London, UK, 1998.
23. Brandt, W. Positron Annihilation in Molecular Substances and Ionic Crystals. In *Positron Annihilation*; Steward, A.T., Roellig, L.O., Eds.; Academic Press: New York, NY, USA, 1967; pp. 155–182.
24. Wang, T.-M.; Shimotomai, M.; Doyama, M. Study of vacancies in the intermetallic compound Ni<sub>3</sub>Al by positron annihilation. *J. Phys. F Met. Phys.* **1984**, *14*, 37–45. [[CrossRef](#)]
25. Perminov, D.A.; Druzhkov, A.P.; Arbutov, V.L. Positron-annihilation studies of the influence of nanodimensional intermetallic precipitates on the evolution of radiation defects in the Fe–Ni–Al alloy. *Phys. Met. Metallogr.* **2015**, *116*, 1151–1158. [[CrossRef](#)]

26. Melikhova, O.; Kuriplach, J.; Prochazka, I.; Cizek, J.; Hou, M.; Zhurkin, E.; Pisov, S. Simulation of positron annihilation response to mechanical deformation of nanostructured Ni<sub>3</sub>Al. *Appl. Surf. Sci.* **2008**, *255*, 157–159. [[CrossRef](#)]
27. Picasso, A.; Somoza, A.; Tolley, A. Nucleation, growth and coarsening of  $\gamma'$ -precipitates in a Ni–Cr–Al-based commercial superalloy during artificial aging. *J. Alloy Compd.* **2009**, *479*, 129–133. [[CrossRef](#)]
28. Macchi, C.E.; Somoza, A.; Santos, G.; Petkov, M.; Lynn, K.G. On the precipitation sequence in a Ni-based superalloy: A Coincidence Doppler Broadening study. *Phys. Stat. Sol. (C)* **2007**, *4*, 3542–3545. [[CrossRef](#)]
29. Sims, C.T. Prediction of phase composition. In *Superalloys II*; Sims, C.T., Staloff, N., Hagel, W.C., Eds.; John Wiley & Sons: New York, NY, USA, 1987; pp. 217–240.
30. Caron, P.; Tasadduq, K. Evolution of Ni-based superalloys for single crystal gas turbine blade applications. *Aerosp. Sci. Technol.* **1999**, *3*, 513–523.
31. Jacques, A.; Trehorel, R.; Schenk, T. High-temperature dislocation climb in the  $\gamma'$  rafts of single-crystal superalloys: The hypothesis of a control by dislocation entry into the rafts. *Met. Mater. Trans. A* **2018**, *49*, 4110–4125. [[CrossRef](#)]
32. Austin, C.M.; Darola, R.; O'Hara, K.S.; Ross, E. General Electric Company. U.S. Patent 5151249, 29 September 1992.
33. Reed, R.C. *The Superalloys, Fundamentals and Applications*; Cambridge University Press: Cambridge, UK, 2006.
34. Kansy, J. Microcomputer program for analysis of positron annihilation lifetime spectra. *Nuclear Instrum. Methods Phys. Res. A* **1996**, *374*, 235–244. [[CrossRef](#)]
35. Bogdanowicz, W. Martensitic transformation in  $\beta$ 1-CuZnAl single crystals studied by X-ray topography method. *Scr. Mater.* **1997**, *37*, 829–835. [[CrossRef](#)]
36. Jirásková, Y.; Schneeweiss, O.; Šob, M.; Novotny, I. Defect and atomic ordering studies in highly deformed and disordered Fe<sub>72</sub>Al<sub>28</sub> alloy. *Acta Metall.* **1997**, *45*, 2147–2154. [[CrossRef](#)]
37. Melikhova, O.; Čížek, J.; Kuriplach, J.; Procházka, I.; Cieslar, M.; Anwand, W.; Brauerb, G. Positron annihilation study of vacancies in Fe–Al based alloys. *Intermetallics* **2010**, *18*, 592–598. [[CrossRef](#)]
38. Schaefer, H.E.; Würschum, R.; Šob, M.; Zák, T.; Yu, W.Z.; Eckert, W.; Banhart, F. Thermal vacancies and positron-lifetime measurements in Fe<sub>76.3</sub>Al<sub>23.7</sub>. *Phys. Rev. B* **1990**, *41*, 11869–11874. [[CrossRef](#)]
39. de Diego, N.; Plazaola, F.; Jiménez, J.A.; Serna, J.; de Rio, J. A positron study of the defect structures in the D0<sub>3</sub> and B2 phases in the Fe–Al system. *Acta Mater.* **2005**, *53*, 163–172. [[CrossRef](#)]
40. Huo, M.; Liu, L.; Yang, W.; Li, Y.; Hu, S.; Su, H.; Zhang, J.; Fu, H. Formation of low-angle grain boundaries under different solidification conditions in the rejoined platforms of Ni-based single crystal superalloys. *J. Mater. Res.* **2018**. [[CrossRef](#)]
41. Sun, D.; Liu, L.; Huang, T.; Yang, W.; Li, Y.; Yue, Q.; Zhang, J.; Fu, H. Insight of the dendrite deformation in Ni-based superalloys for increased misorientation along convergent boundaries. *Prog. Nat. Sci. Mater. Int.* **2018**, *28*, 489–495. [[CrossRef](#)]
42. Epishin, A.I.; Link, T.; Noltze, G.; Svetlov, I.L.; Bokshstein, B.S.; Rodin, A.O.; Salivan-Neumann, R.; Oder, G. Diffusion processes in multicomponent nickel-base superalloy-nickel system. *Phys. Met. Metallogr.* **2014**, *115*, 21–29. [[CrossRef](#)]
43. Anderson, P.M.; Hirth, J.P.; Lothe, J. *Theory of Dislocations*; Cambridge University Press: Cambridge, UK, 2017.
44. Husseini, N.S.; Kumah, D.P.; Yi, J.Z.; Torbet, C.J.; Arms, D.A.; Dufresne, E.M.; Pollock, T.M.; Jones, J.W.; Clarke, R. Mapping single-crystal dendritic microstructure and defects in nickel-base superalloys with synchrotron radiation. *Acta Mater.* **2008**, *56*, 4715–4723. [[CrossRef](#)]

